

Adaptive Compressive Sampling for Mid-infrared Spectroscopic Imaging

Mahsa Lotfollahi, Nguyen Tran, Chalapathi Gajjela, Sebastian Berisha, Zhu Han, David Mayerich, Rohith Reddy.

Mid-infrared spectroscopic imaging (MIRSI) is an emerging class of label-free, biochemically quantitative technologies targeting digital histopathology. Conventional histopathology relies on chemical stains that alter tissue color. This approach is qualitative, often making histopathologic examination subjective and difficult to quantify. MIRSI addresses these challenges through quantitative and repeatable imaging that leverages native molecular contrast. Fourier transform infrared (FTIR) imaging, the best known MIRSI technology, has two challenges that have hindered its widespread adoption: data collection speed and spatial resolution. Recent technological breakthroughs, such as photothermal MIRSI, provide an order of magnitude improvement in spatial resolution. However, this comes at the cost of acquisition speed, which is impractical for clinical tissue samples. This paper introduces an adaptive compressive sampling technique to reduce hyperspectral data acquisition time by an order of magnitude by leveraging spectral and spatial sparsity. This method identifies the most informative spatial and spectral features, integrates a fast tensor completion algorithm to reconstruct megapixel-scale images, and demonstrates speed advantages over FTIR imaging while providing spatial resolutions comparable to new photothermal approaches.

Index Terms—Compressive Sampling, Compressive Sensing, Image Reconstruction, LASSO Reconstruction, Spectroscopic Imaging, SVM Classification Metric

I. INTRODUCTION

MID-INFRARED spectroscopic imaging (MIRSI) is an emerging class of quantitative label-free molecular identification technologies impacting several fields, including histopathology [1], material science [2], environmental and toxicological chemistry [3], and forensics [4]. Fourier transform infrared (FTIR) spectroscopic imaging is the best known MIRSI technique that provides spatially resolved images of molecular constituents. FTIR imaging probes the sample with mid-infrared light (2.5 to 12.5 μm), and has a wavelength λ dependant, diffraction limited spatial resolution [5]. While this resolution is sufficient for numerous applications, it limits the applicability of MIRSI in several fields such as cellular and sub-cellular microscopy, where features are smaller than $\approx 6\mu\text{m}$ in size.

New MIRSI technologies such as photothermal infrared (PTIR) [6] and optical photothermal infrared (O-PTIR) [7] spectroscopy overcome the FTIR diffraction limit using a pump-probe instrumentation architecture. The sample is excited using a mid-infrared quantum cascade laser source, and localized absorbance is measured using an atomic force microscope [6] or secondary optical beam with a smaller resolution [7]. These techniques provide sub-micrometer resolution but slow at obtaining hyperspectral data on large samples. For example, O-PTIR imaging of a 1 mm² sample at 250 nm pixel spacing, which is typical in histology, requires approximately 46 days using current instrumentation.

We hypothesize that acquisition time can be dramatically reduced using compressive sampling [8] to take advantage of spatial and spectral sparsity inherent in MIRSI data [9]. Instrumentation for O-PTIR is versatile and allows for ac-

quisition of (1) a 1D spectrum or (2) a 2D band image at one wavenumber in one measurement. We will utilize this versatility along with sparsity based reconstructions to achieve an order of magnitude improvement in data collection speed.

In this paper, we describe an adaptive method to identify the most informative spatial and spectral features given the O-PTIR sampling constraints. We then simulate data acquisition on large FTIR images and reconstruct the resulting hyperspectral image (HSI) using a fast tensor completion algorithm to handle megapixel-scale hyperspectral data. This allows us to directly compare our reconstruction results to the underlying ground truth data and validate our algorithm. We also demonstrate that the most common metrics used to quantify reconstructed HSI quality are inadequate *in practice*. We therefore propose a classification-based metric compatible with FTIR image assessment.

II. COMPRESSIVE SENSING

Compressive sensing (CS) is extensively employed in digital image and signal processing [10], [11], [12] to reduce data throughput by leveraging sparse optimization to reconstruct incomplete measured data [8]. CS theory [13] utilizes the fact that objects being imaged have a sparse representation in some basis. FTIR spectra are sparse when projected on a principal component [14] or Fourier bases [15].

In this paper, we reconstruct a large hyperspectral data cube with the size of $N_S \times Z_S$ using N_D selected point spectra ($N_D \ll N_S$) and Z_D spectral band images ($Z_D \ll Z_S$) selected in different wavenumbers, where $N_S = X_S \times Y_S$ is the number of pixels in spatial domain and Z_S is the number of spectral bands in the reconstructed hyperspectral data.

III. ADAPTIVE SAMPLING

Our approach uses an iterative method of adaptive sampling and image reconstruction. At each iteration, identify and

This work was supported in part by the NLM Training Program in Biomedical Informatics and Data Science T15LM007093 (RM, RR), the Cancer Prevention and Research Institute of Texas (CPRIT) #RR170075 (RR), National Institutes of Health #R01HL146745 (DM), and the National Science Foundation CAREER Award #1943455 (DM).

collect the most informative band images and point spectra. This new data is then integrated into a reconstruction used to inform sampling in the next iteration.

We proposed an iterative method to select point spectra and band images to provide a basis for optimally reconstructing the hyperspectral volume. We initiate the process with taking the band image at Amide I (1654 cm^{-1}) which provides the most molecular information for biological samples (Fig. 1a). Then we apply Simple Linear Iterative Clustering (SLIC) [16] to perform a local clustering of pixels. SLIC clusters pixels into the desired number of superpixels (N) based on their color, similarity and proximity in the image plane (Fig. 1b). The center of superpixels are considered as the position of point spectra (Fig. 1c). Selecting the new positions of point spectra and a new single band image is done alternatively (Fig. 1d-e). The second band image is chosen based on the first band image and the point spectra. We compute the spectral correlation coefficient between the first selected band and all original bands from the taken point spectra. The band with lowest correlation coefficient is the most uncorrelated informative band. The noise components have low magnitude but they may look more different (uncorrelated) than others. Then the optimal band should have the highest uncorrelation with the first band and highest magnitude. Having two band images, the SLIC algorithm is applied to find more points in spatial domain for taking spectra. The rest of band selection is initialized with a pair of bands $B_1 = 1654 \text{ cm}^{-1}$ and B_2 , followed by the orthogonal subspace projection (OSP) algorithm [17]. Before applying OSP, the bands with low SNR and the ones corresponding to water absorption should be removed. Those bands can be selected by computing the spectral correlation coefficient matrix between the original bands. The bands with low correlation with the adjacent bands (low value in upper diagonal of correlation coefficient matrix) carry unrelated information (noise) and should be excluded.

The initial set of selected sub-bands is defined as $\Phi_0 = \{B_1, B_2\}$. The next band B_3 should provide the maximum amount of additional information, and is therefore selected to be the most *dissimilar* to Φ_0 . B_3 therefore has the maximum projection on the orthogonal subspace of B_1 and B_2 .

$$\mathbf{P} = \mathbf{I} - \mathbf{Z}(\mathbf{Z}^T \mathbf{Z})^{-1} \mathbf{Z}^T$$

where \mathbf{Z} is an $N \times 2$ matrix where the N -pixel columns represent the $\sqrt{N} \times \sqrt{N}$ band images B_1 and B_2 respectively. The projection of all selected points ($y^{N \times 1}$) in band (B) on the orthogonal subspace of Φ are computed:

$$y_0 = \mathbf{P}^T y$$

The band with the maximum orthogonal component $\|y_0\|$ is the most dissimilar, therefore Φ is updated to include the new band image: $\Phi_1 = \{B_1, B_2, B_3\}$. This process continues after selecting additional point spectra to exploit all available information. New spectral bands are iteratively selected until the desired threshold is reached.

IV. RECONSTRUCTION

We use a hyperspectral fusion algorithm with a LASSO optimizer [18]. This algorithm requires two inputs to gen-

erate a high resolution hyperspectral image. The first input $\mathbf{H} \in \mathbb{R}^{N_D \times Z_S}$ consists of full spectra at N_D selected points. The second input $\mathbf{M} \in \mathbb{R}^{N_S \times Z_D}$ consists of images at selected spectral bands. Our goal is to leverage a small number of spectral and spatial samples, such that $N_D \ll N_S$ and $Z_D \ll Z_S$, to generate a fusion image $\mathbf{S} \in \mathbb{R}^{N_S \times Z_S}$ with high resolution in *both* spectral and spatial domains.

A. Image Generation

Image \mathbf{H} is represented as:

$$\mathbf{H} = \mathbf{L}\mathbf{S} + \eta_1, \quad (1)$$

where $\mathbf{L} \in \mathbb{R}^{N_D \times N_S}$ is an operator to re-sample \mathbf{S} . Similarly, image \mathbf{M} is generated by:

$$\mathbf{M} = \mathbf{S}\mathbf{B} + \eta_2, \quad (2)$$

where $\mathbf{B} \in \mathbb{R}^{Z_S \times Z_D}$ is a sparse matrix that extract individual bands from \mathbf{S} . Both η_1 and η_2 are assumed to be additive white Gaussian noise. The next step is PCA where the fusion image is defined as $\mathbf{S} = [s_1, \dots, s_{N_S}]^T$. Each rows of vector $\mathbf{s}_i = [s_{i,1}, s_{i,2}, \dots, s_{i,Z_S}]$ contains all the spectral information at a spatial pixel location. We represent \mathbf{s}_i in subspace \mathbf{Q} as:

$$\mathbf{s}_i = \mathbf{r}_i \mathbf{Q}, \quad (3)$$

where $\mathbf{r}_i \in \mathbb{R}^{1 \times \tilde{Z}}$ is the projection of \mathbf{s}_i onto the orthonormal subspace spanned by the columns of $\mathbf{Q} \in \mathbb{R}^{\tilde{Z} \times Z_S}$, such that $\tilde{Z} \ll Z_S$. The image $\mathbf{R} \in \mathbb{R}^{N_S \times \tilde{Z}}$ projected onto this subspace is composed of the reduced spectras: $\mathbf{R} = [\mathbf{r}_1, \dots, \mathbf{r}_{N_S}]^T$. Integrating (Eqn. 3) into (Eqn. 1) and (Eqn. 2), we can express \mathbf{H} and \mathbf{M} as:

$$\mathbf{H} = \mathbf{L}\mathbf{R}\mathbf{Q} + \eta_1, \quad (4)$$

$$\mathbf{M} = \mathbf{R}\mathbf{Q}\mathbf{B} + \eta_2. \quad (5)$$

B. Initialization

$\bar{\mathbf{R}}$ is the initialization of \mathbf{R} using Maximum a Posteriori (MAP) and it is defined as:

$$\bar{\mathbf{R}} = \left(\mathbf{Q}^T \mathbf{L}^T \mathbf{\Lambda}_H \mathbf{L} \mathbf{Q} + \mathbf{\Lambda}_{\bar{\mathbf{R}}|\mathbf{M}} \right)^{-1} \left(\mathbf{L}^T \mathbf{\Lambda}_H \mathbf{Q}^T \mathbf{H} + \mathbf{\Lambda}_{\bar{\mathbf{R}}|\mathbf{M}}^{-1} \bar{\mathbf{R}} \right). \quad (6)$$

where

- $\bar{\mathbf{R}} = \mathbb{E}\{\bar{\mathbf{R}}|\mathbf{M}\}$ is the expected value of $\bar{\mathbf{R}}$ given \mathbf{M} ,
- Rewrite as: $\bar{\mathbf{R}} = \mathbb{E}(\bar{\mathbf{R}}) + \frac{\mathbf{\Lambda}_{\bar{\mathbf{R}},\mathbf{M}}[\mathbf{M} - \mathbb{E}(\mathbf{M})]}{\mathbf{\Lambda}_{\mathbf{M},\mathbf{M}}}$,
- $\mathbf{\Lambda}_{\bar{\mathbf{R}},\mathbf{M}}$ is the cross-covariance matrices with form: $\mathbf{\Lambda}_{\bar{\mathbf{R}},\mathbf{M}} = \mathbb{E}[(\bar{\mathbf{R}} - \mathbb{E}(\mathbf{M}))(\bar{\mathbf{R}} - \mathbb{E}(\mathbf{M}))^T]$,
- $\mathbf{\Lambda}_{\bar{\mathbf{R}}|\mathbf{M}}$ is the row covariance matrix of $\bar{\mathbf{R}}$ given \mathbf{M} as: $\mathbf{\Lambda}_{\bar{\mathbf{R}}|\mathbf{M}} = \mathbf{\Lambda}_{\bar{\mathbf{R}},\bar{\mathbf{R}}} - \frac{\mathbf{\Lambda}_{\bar{\mathbf{R}},\mathbf{M}} \mathbf{\Lambda}_{\bar{\mathbf{R}},\mathbf{M}}^T}{\mathbf{\Lambda}_{\mathbf{M},\mathbf{M}}}$.

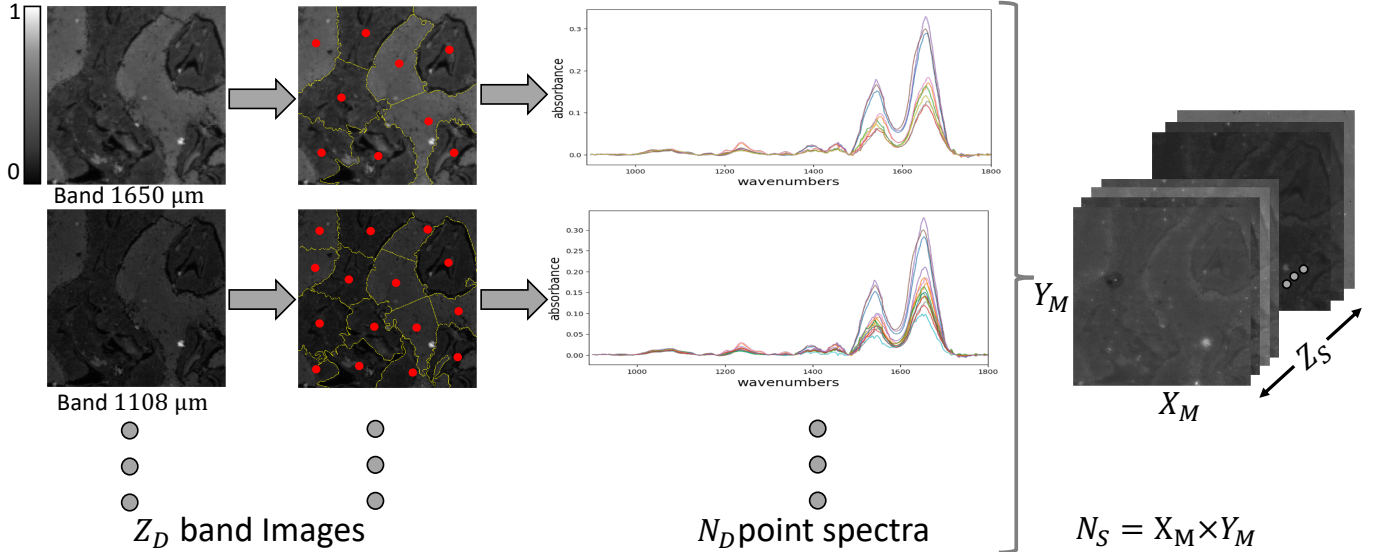


Fig. 1. Adaptive Sampling using the iterative method. Each row, columns left to right; first column: The selected band image. Second column: The clustered image using SLIC, center of superpixels are specified as red circles. Third column: IR spectra at the center of superpixels. By integrating $Z_D \ll Z_S$ band images and $N_D \ll N_S$ point spectra, the high resolution hyperspectral image ($N_S \times Z_S$) is reconstructed using the proposed method (the right-hand side image)

C. Least Absolute Shrinkage and Selection Operator (LASSO)

In the next step, LASSO is implemented to solve for \mathbf{R} in Equation (4) and (5). The optimization equation is as follow:

$$\arg \min_{\mathbf{R}} \frac{1}{2} \left\| \mathbf{\Lambda}_H^{-\frac{1}{2}} (\mathbf{H} - \mathbf{L}\mathbf{R}\mathbf{Q}) \right\|_F^2 + \frac{1}{2} \left\| \mathbf{\Lambda}_M^{-\frac{1}{2}} (\mathbf{M} - \mathbf{R}\mathbf{Q}\mathbf{B}) \right\|_F^2 + \eta \|\mathbf{R}\|_n. \quad (7)$$

In the final step, ADMM is implemented to solve Equation 7 [18].

V. RESULTS

The proposed reconstruction method is applied on FTIR hyperspectral data in high magnification mode from TMA BR961 using the Agilent Stingray imaging system. The imaging system is composed of a Cary 680 spectrometer coupled to a Cary 620 microscope with 0.62 numerical aperture, projected pixel size of $1.1 \mu\text{m}$ and spectral resolution of 8cm^{-1} . We truncated the spectral range between 900 to 1800cm^{-1} to be the same range of photothermal spectroscopy.

To reconstruct a single core with the size of $1380 \times 1380 \times 117$ from the TMA96, our algorithm requires a few number of high resolution band images and some point spectra. The process begins with acquiring the first band image at 1654cm^{-1} . In each iteration, an extra single band is added based on band selection described in "Adaptive Sampling" section. Then SLIC is applied on the available band images to extract desired number of superpixels. The center of superpixels are the position of point spectra. At the beginning, we specify the number of point spectra to be 20, 40, 80, 160, 240, 480 in each iteration respectively. However, the numbers of actually generated superpixels is not equal to those given numbers due updating the initialized centers as the lowest gradient position

TABLE I
PERFORMANCE METRICS AND CLASSIFICATION ACCURACY IN EACH ITERATION BY ADDING ONE BAND IMAGE AND GIVEN NUMBER OF POINT SPECTRA.

#Iter	#Point Spectra	Selected Wavenumbers	Performance Metrics				RBF SVM Accuracy
			PSNR	RMSE	SAM	ERGAS	
1	14	1654	21.86	0.0806	2.1465	14.807	18%
2	40	1654, 991	44.14	0.0062	0.462	1.072	49%
3	68	1654, 991, 1623	45.34	0.0054	0.363	0.955	45%
4	192	1654, 991, 1623, 1562	45.15	0.0055	0.317	0.992	75%
5	378	1654, 991, 1623, 1562, 1153	46.33	0.0048	0.267	0.868	94%
6	771	1654, 991, 1623, 1562, 1153, 1083	49.60	0.0033	0.222	0.590	94%

in a corresponding local neighborhoods [19]. A smoothing Gaussian kernel with $\sigma = 5$ is applied prior to clustering and the compactness factor is set to be 0.03.

We compare the original and reconstructed image in each iteration using multiple performance metrics including, peak signal to noise ratio (PSNR), Root Mean Square Error (RMSE), Spectral Angle Mapper (SAM) and Relative Dimensionless Global Error (ERGAS) [20], [21], [22], [23]. In addition, to make sure that the reconstructed data can capture all biological features, support vector machines (SVM) with radial basis function (RBF) kernel is used to identify six major cellular and acellular constituents of tissue, namely adipocytes, blood, collagen, epithelium, necrosis, and myofibroblasts. The RBF SVM classifier is trained using 10,000 pixels per class from TMA BR961 [24]. RBF SVM provides overall accuracy of 94% on a test FTIR breast core. This core has been used for reconstruction validation as well.

The reconstructed data is evaluated using multiple, previously published metrics (Table I). Reconstruction after two iterations generates high quality output based on metrics such as PSNR and RMSE. However, the low classification accuracy indicates that the molecular content is not accurately reconstructed. After five iterations, using 5 band images and 378 point spectra, the classification accuracy saturates at 94% and is comparable to the accuracy for raw data (Fig. 2). The

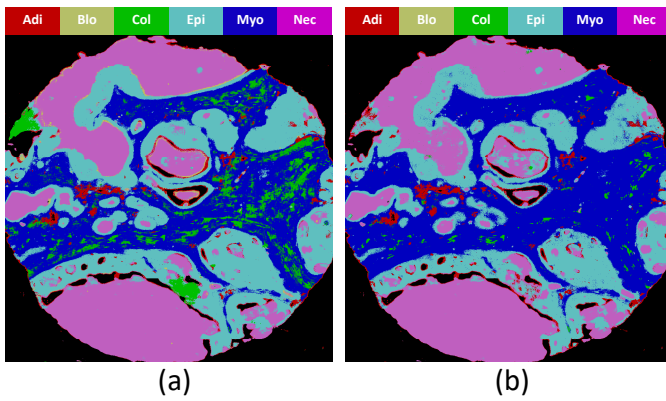


Fig. 2. RBF SVM classification on the original FTIR breast core (a) and the reconstructed core using the proposed method (b).

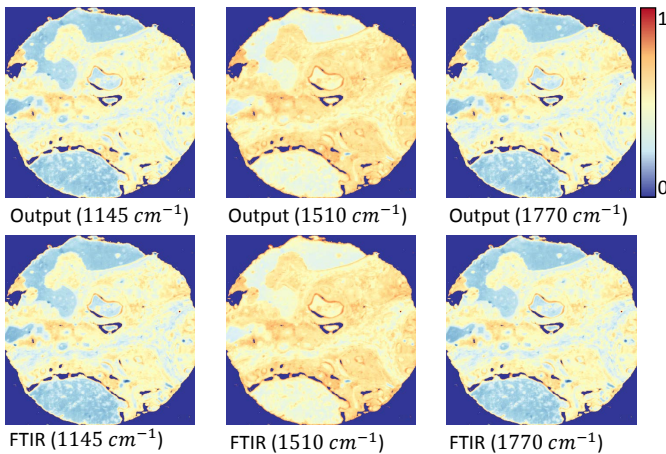


Fig. 3. Infrared image of breast tissue biopsy in different wavenumbers. Top row: the reconstruction results using 5 band images and 378 point spectra. Bottom row: the original FTIR data (ground truth).

reconstructed and raw data in Fig. 3 at multiple wavenumbers show good correspondence. Moreover, Table I shows that the reconstructed data at all 117 bands and 1,904,400 pixels is nearly identical to the raw data using multiple metrics.

VI. CONCLUSION

We propose an approach for reconstructing hyperspectral images using methods compatible with new high-resolution imaging instruments. The reconstructions require less than 5% of the original data by leveraging sparsity in both the spectral and spatial dimensions. The proposed algorithm selects the most informative individual spectra and band images. Sparse reconstruction image is done through weighted LASSO tensor completion. In addition to validating our approach using conventional metrics, we also propose using tissue classification as an alternative criterion. This approach more heavily weights the ability to distinguish critical molecular constituents, making the final reconstruction more useful for biochemical differentiation.

REFERENCES

[1] S. Pahlow, K. Weber, J. Popp, R. W. Bayden, K. Kochan, A. R  ther, D. Perez-Guaita, P. Heraud, N. Stone, A. Dudgeon *et al.*, "Application

of vibrational spectroscopy and imaging to point-of-care medicine: A review," *Applied spectroscopy*, vol. 72, no. 101, pp. 52–84, 2018.

[2] J.-L. Xu, K. V. Thomas, Z. Luo, and A. A. Gowen, "Ftir and raman imaging for microplastics analysis: State of the art, challenges and prospects," *TrAC Trends in Analytical Chemistry*, vol. 119, p. 115629, 2019.

[3] J. Trevisan, P. P. Angelov, P. L. Carmichael, A. D. Scott, and F. L. Martin, "Extracting biological information with computational analysis of fourier-transform infrared (ftir) biospectroscopy datasets: current practices to future perspectives," *Analyst*, vol. 137, no. 14, pp. 3202–3215, 2012.

[4] V. Sharma and R. Kumar, "Ftir and nirs in forensic chemical sensing," in *Forensic Analytical Methods*, 2019, pp. 164–197.

[5] R. K. Reddy, M. J. Walsh, M. V. Schulmerich, P. S. Carney, and R. Bhargava, "High-definition infrared spectroscopic imaging," *Applied spectroscopy*, vol. 67, no. 1, pp. 93–105, 2013.

[6] S. Bialkowski, *Photothermal spectroscopy methods for chemical analysis*. John Wiley & Sons, 1996, vol. 134.

[7] D. Zhang, C. Li, C. Zhang, M. N. Slipchenko, G. Eakins, and J.-X. Cheng, "Depth-resolved mid-infrared photothermal imaging of living cells and organisms with submicrometer spatial resolution," *Science advances*, vol. 2, no. 9, p. e1600521, 2016.

[8] E. J. Candès and M. B. Wakin, "An introduction to compressive sampling [a sensing/sampling paradigm that goes against the common knowledge in data acquisition]," *IEEE signal processing magazine*, vol. 25, no. 2, pp. 21–30, 2008.

[9] B. Deutsch, R. Reddy, D. Mayerich, R. Bhargava, and P. S. Carney, "Compositional prior information in computed infrared spectroscopic imaging," *JOSA A*, vol. 32, no. 6, pp. 1126–1131, 2015.

[10] J. Ender, "A brief review of compressive sensing applied to radar," in *2013 14th International Radar Symposium (IRS)*, vol. 1. IEEE, 2013, pp. 3–16.

[11] R. M. Willett, R. F. Marcia, and J. M. Nichols, "Compressed sensing for practical optical imaging systems: a tutorial," *Optical Engineering*, vol. 50, no. 7, p. 072601, 2011.

[12] W. L. Chan, M. L. Moravec, R. G. Baraniuk, and D. M. Mittleman, "Terahertz imaging with compressed sensing and phase retrieval," *Optics letters*, vol. 33, no. 9, pp. 974–976, 2008.

[13] E. Candès and J. Romberg, "l1-magic: Recovery of sparse signals via convex programming," *URL: www.acm.caltech.edu/l1magic/downloads/l1magic.pdf*, vol. 4, p. 14, 2005.

[14] R. K. Reddy and R. Bhargava, "Accurate histopathology from low signal-to-noise ratio spectroscopic imaging data," *Analyst*, vol. 135, no. 11, pp. 2818–2825, 2010.

[15] T. H. Nguyen, R. K. Reddy, M. J. Walsh, M. Schulmerich, G. Popescu, M. N. Do, and R. Bhargava, "Denoising and deblurring of fourier transform infrared spectroscopic imaging data," in *Computational Imaging X*, vol. 8296. International Society for Optics and Photonics, 2012, p. 82960M.

[16] R. Achanta, A. Shaji, K. Smith, A. Lucchi, P. Fua, and S. S  sstrunk, "Slic superpixels," *Tech. Rep.*, 2010.

[17] Q. Du and H. Yang, "Similarity-based unsupervised band selection for hyperspectral image analysis," *IEEE Geosci. Remote Sensing Lett.*, vol. 5, no. 4, pp. 564–568, 2008.

[18] N. Tran, R. Mankar, D. Mayerich, and Z. Han, "Hyperspectral-Multispectral Image Fusion with Weighted LASSO," *arXiv e-prints*, p. arXiv:2003.06944, Mar. 2020.

[19] H. Wang, X. Peng, X. Xiao, and Y. Liu, "Bslc: Slic superpixels based on boundary term," *Symmetry*, vol. 9, no. 3, p. 31, 2017.

[20] L. Wald, "Quality of high resolution synthesised images: Is there a simple criterion?" 2000.

[21] P. Jagalingam and A. V. Hegde, "A review of quality metrics for fused image," *Aquatic Procedia*, vol. 4, pp. 133–142, 2015.

[22] U. Sara, M. Akter, and M. S. Uddin, "Image quality assessment through fsim, ssim, mse and psnr—a comparative study," *Journal of Computer and Communications*, vol. 7, no. 3, pp. 8–18, 2019.

[23] S. Kavitha and K. Thyagarajan, "A survey on quantitative metrics for assessing the quality of fused medical images," *Research Journal of Applied Sciences, Engineering and Technology*, vol. 12, no. 3, pp. 282–293, 2016.

[24] S. Berisha, M. Lotfollahi, J. Jahanipour, I. Gurcan, M. Walsh, R. Bhargava, H. Van Nguyen, and D. Mayerich, "Deep learning for ftir histology: leveraging spatial and spectral features with convolutional neural networks," *Analyst*, vol. 144, no. 5, pp. 1642–1653, 2019.